Supplymentary Notes

Supplementary Note S1 | Sample fabrication

We exfoliated graphene by tape from Kish graphite and also grew graphene by chemical vapor deposition (CVD) on Cu substrate. Then we fabricated SiO_2-supported and suspended graphene samples by two steps: (1) nanofabrication of the Si wafer; (2) graphene transfer onto the Si wafer with holes. Firstly, we etched 10 μm deep holes with various diameters on the 1 cm×1 cm Si wafer by photolithography and anisotropic dry etching. Next, the exfoliated graphene was mechanically transferred onto the Si wafer with the help of the tape and the CVD-grown graphene was transferred with the help of PMMA. The PMMA layer was spin coated onto the as-CVD-grown graphene on copper where the copper coil was then etched by Fe^{+3} solution. The PMMA/graphene layers were transferred onto the Si wafer and the PMMA layer was removed by acetone vapor, leaving large-area graphene partly suspended over holes and partly supported on SiO_2.

Supplementary Note S2 | Spreading thermal resistance of the underlying Si layer and evaluation of laser heating in the substrate

For the SiO_2-supported graphene samples, the total thermal resistance in the thickness direction consists of the thermal resistance of the graphene-SiO_2 interface, the SiO_2 layer and the Si layer. The spreading thermal resistance of the 500μm-thick Si layer is approximately $R_{Si}\approx 1/(4\pi\lambda_{Si}r_0)$ [1] where λ_{Si} is the thermal conductivity of silicon (148 W/(m·K)), the vertical thermal resistance of the 300nm-thick SiO_2 layer is estimated as $R_{ox}\approx L/(\lambda_b\pi r_0^2)$ and the interfacial thermal resistance is $R_i\approx 1/(g\pi r_0^2)$. Taking r_0 = 500 nm and g = 0.1 ~ 9 MW/(m^2·K) as measured, the thermal resistances of the Si layer, SiO_2 layer and the interface are calculated to be 1.1×10^3 K/W, 2.6×10^5 K/W and 1.4×10^5 ~ 1.3×10^7 K/W, respectively. Therefore, the thermal resistance of the interface is 0.54 ~ 50 times of that of the SiO_2 layer and the total thermal resistance of the interface and the SiO_2 layer is 3.6×10^2 ~ 1.2×10^4 times of the spreading thermal resistance of the Si layer. Thus the spreading thermal resistance of the Si layer is negligible and we only considered the graphene/SiO_2 layers in the heat conduction model for the supported samples.

Next, we evaluate the effect of laser heating in the substrate. The optical absorptivity of SiO_2 and Si were respectively ~10^{-5} and 0.6 [2], thus the laser absorption in SiO_2 is negligible while the laser heating in Si needs to be evaluated. The absorption length of Si at 488nm is less than 1μm, so we consider a point heat source model with the spreading thermal resistance $R_{Si}\approx 1/(4\pi\lambda_{Si}r_0)$. Moreover, we assume that the laser absorptivity of monolayer graphene is 0.023 and that the laser is reflected at the SiO_2/Si interface by 40%, and the laser absorptivity of 4-layer graphene is further calculated to be 0.089. We use $\theta_{g,Si}$ to denote the temperature rise in graphene induced by laser heating in Si, and $\theta_{g,g}$ to denote the temperature rise in graphene induced by its own laser absorption. Based on the thermal resistance circuit described in the previous paragraph, the ratio of $\theta_{g,Si}$ to $\theta_{g,g}$ is calculated to be 0.04% for the supported 4-layer graphene sample (g = 0.11 MW/(m^2·K)) and 5% for the supported monolayer sample (g = 9.0 MW/(m^2·K)). In our data analysis, we used the normalized temperature rise to extract the thermal properties, and thus the uncertainty from substrate heating is calculated to be trivial for the supported 4-layer sample and within 2% for the supported monolayer sample. Therefore, it is reasonable to set the boundary

condition at the SiO_2/Si interface as zero temperature rise. In the literature, Judek et al. (Ref. [39] in the manuscript) detected the temperature rise of the Si surface when they used laser to heat graphene supported on Si/285nm-SiO_2 (g = 1.99 MW/(m^2·K)), showing that the temperature rise of Si surface is within the temperature measurement uncertainty, so they also took zero temperature rise at the SiO_2/Si surface.

Supplementary Note S3 | Evaluation of temperature rise induced by the calibration laser power

During the calibration of the temperature dependence of 2D band shifts, in order to avoid significant temperature increase in the sample, we used 1.3 mW incident laser power with a relatively large spot size (laser spot radius≈1.5μm) and performed the calibration in air. Here we demonstrate that the laser induced temperature rise during the calibration process is negligible by analyzing the experimental data of a large suspended sample. Fig. S1(a) shows the 2D band shifts of the suspended 6μm-diameter sample as a function of the incident laser power obtained in vacuum at 30℃ with r_0 = 243 nm, and the intercept of the linear fitting shows that the 2D band shift is 2736.21 cm^{-1} at zero laser power. Fig. S1(b) shows the calibrated 2D band shift as a function of the stage temperature, which gives a negatively linear relationship between the 2D band shift and temperature. In this calibration, the 2D band shift at 30℃ (2737.7±0.4 cm^{-1}) is even larger than the zero-laser-power intercept of 2736.21 cm^{-1} in Fig. S1(a), indicating that the temperature increase during the calibration process is within the temperature measurement uncertainty limit.

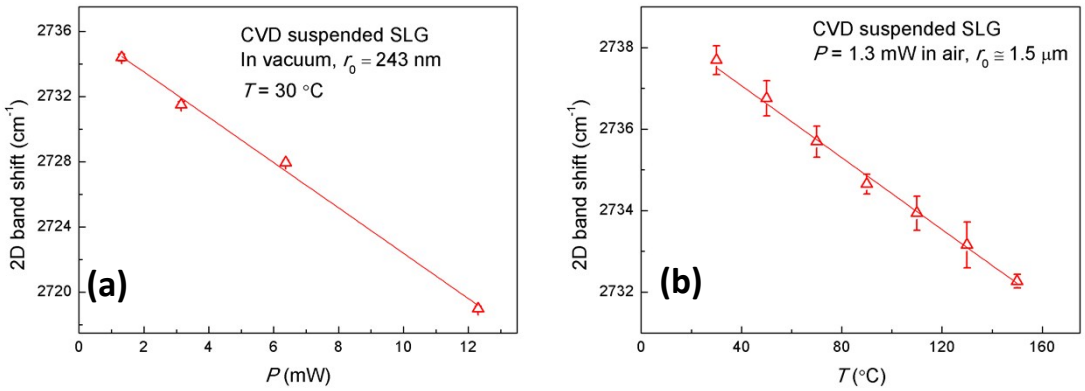

FIGURE S1. Raman 2D band shifts of the suspended CVD monolayer graphene sample with 6μm diameter as a function of (a) the incident laser power and (b) the stage temperature.

Moreover, the laser power was changed with optical filters in all of our temperature measurements, and the difference between two band shifts at two incident laser powers, $\omega = \omega_1 - \omega_2$, is used to calculate the temperature rise due to the difference of laser power, $P = P_1 - P_2$ (P_2 is a very low power or the zero-laser-power intercept). Instead of using the absolute value of the calibrated band shift, the slope of $d\omega/dT$ is used to calculate the temperature rise by $\Delta T = (\omega_1 - \omega_2)\, dT/d\omega$, and the value of the $d\omega/dT$ slope is independent of the small temperature rise during the calibration process. Therefore, the uncertainty from the temperature rise due to calibration laser heating is negligible.

Supplementary Note S4 | Analytical solution for the temperature rise of supported graphene

Eqs. (1) – (5) for the supported graphene were analytically solved by successively applying Hankel and Laplace transforms. The temperature rise induced by the pulsed laser heating can be divided into the steady-state and time-dependent parts; that is,

$$\theta_{\text{sup}}(r,t)=\theta_{\text{sup,st}}(r)+\theta_{\text{sup,tr}}(r,t) \quad \text{S(1)}$$

where $\theta_{\text{sup,st}}$ is the steady-state temperature rise for CW laser heating and $\theta_{\text{sup,tr}}$ is the time-dependent part. The Raman-measured temperature rise is the Gaussian-weighted-average steady-state temperature rise and its analytical expression is given as

$$\overline{\theta_{\text{sup,st}}(r)}=\eta' P\sum_{n=1}^{\infty}\frac{2q^{*}(r_0;\mu_n)^2}{\pi r_0^4}f_{1n}(\lambda_{\text{sup}},g;\mu_n) \quad \text{S(2)}$$

where q^* is the Hankel transform function of the Gaussian function, expressed as

$$q^{*}(r_0;\mu_n)=\int_0^{\infty}H_0(r;\mu_n)\exp\left(-r^2/r_0^2\right)rdr \quad \text{S(3)}$$

where $H_0(r;\mu_n)$ is the kernel function of the Hankel transform:

$$H_0(\mu_n,r)=\frac{\sqrt{2}}{R_0}\frac{J_0(\mu_n x)}{J_1(\mu_n R_0)}\ (R_0\to\infty),\ J_0(\mu_n R_0)=0\ \ (n=1,2,3,\ldots) \quad \text{S(4)}$$

and f_{1n} is a function of λ_{sup} and g:

$$f_{1n}(\lambda_{\text{sup}},g;\mu_n)=\frac{\tanh(\mu_n L)g/(\mu_n\lambda_{\text{b}})+1}{\mu_n^2\lambda_{\text{sup}}b+\mu_n\tanh(\mu_n L)g\lambda_{\text{sup}}b/\lambda_{\text{b}}+g} \quad \text{S(5)}$$

The spatial and time averaged expression for the time-dependent part is given as

$$\overline{\theta_{\text{sup,tr}}(r,t)}=\eta' P\sum_{n=1}^{\infty}\frac{2q^{*}(r_0;\mu_n)^2}{\pi r_0^4}f_{2n}(\lambda_{\text{sup}},g,\alpha_{\text{sup}},t_{\text{h}};\mu_n) \quad \text{S(6)}$$

where f_{1n} is a function of λ_{sup}, g, α_{sup} and t_{h}:

$$f_{2n}(\lambda_{\text{sup}},g,\alpha_{\text{sup}},t_{\text{h}};\mu_n)=\sum_{m=1}^{\infty}\frac{2\omega_m\left[1-\exp\left(-\alpha_{\text{b}}(\omega_m^2+\mu_n^2)t_{\text{h}}\right)\right]}{\alpha_{\text{b}}(\omega_m^2+\mu_n^2)^2}\times\frac{g\tan(\omega_m L)+\lambda_{\text{b}}\omega_m}{Z_{mn}} \quad \text{S(7)}$$

where ω_{m} is the root of $Q_{\text{mn}}(\omega_{\text{m}})=0$:

$$\begin{aligned}Q_{mn}(\omega_m)=&\ g\lambda_{\text{sup}}b\tan(\omega_m L)\left[\alpha_{\text{sup}}\mu_n^2-\alpha_{\text{b}}(\omega_m^2+\mu_n^2)\right]\\&+\omega_m\lambda_{\text{b}}\left[\alpha_{\text{sup}}(g+\lambda_{\text{sup}}b\mu_n^2)-\alpha_{\text{b}}\lambda_{\text{sup}}b(\omega_m^2+\mu_n^2)\right]=0\end{aligned} \quad \text{S(8)}$$

and Z_{mn} is expressed as

$$\begin{aligned}Z_{mn}=\rho c_{\text{p,sup}}&\left[\begin{matrix}\alpha_{\text{b}}Lb(\omega_m^2+\mu_n^2)(\lambda_{\text{b}}\omega_m\tan(\omega_m L)-g)\\-2\omega_m\alpha_{\text{b}}bg\tan(\omega_m L)-\alpha_{\text{b}}\lambda_{\text{b}}b(3\omega_m^2+\mu_n^2)\end{matrix}\right]\\&+g\lambda_{\text{b}}+\lambda_{\text{sup}}b\mu_n^2(Lg+\lambda_{\text{b}})-\lambda_{\text{b}}\omega_m\tan(\omega_m L)L(\mu_n^2\lambda_{\text{sup}}b+g)\end{aligned} \quad \text{S(9)}$$

As seen from the above expressions, the Raman-measured temperature rises in response to both

CW and pulsed lasers are proportional to the laser absorption and change with both laser spot radii and pulse durations, and thus the thermophysical properties can be extracted from the normalized temperature rise curves with no pre-knowledge of laser absorption.

Supplementary Note S5 | Analytical solution for the temperature rise of suspended graphene

As for the suspended graphene, the analytical solution of Eqs. (9) – (11) is obtained by applying Laplace transform. Here we define a characteristic temperature rise as $\theta_{0,\mathrm{sus}} = \eta P/(\pi\lambda_{\mathrm{sus}}b)$ and the dimensionless temperature rise as $T_{\mathrm{sus}} = \theta_{\mathrm{sus}}/\theta_{0,\mathrm{sus}}$, the dimensionless position as $x = r/r_0$ and dimensionless suspending diameter as $x_d = d/r_0$, the dimensionless thermal contact resistance as $\xi = \lambda_{\mathrm{sus}}R_{\mathrm{c}}b$ and the Fourier number as $Fo_{\mathrm{sus}} = \alpha_{\mathrm{sus}}t_{\mathrm{h}}/r_0^2$. The dimensionless temperature rise induced by pulsed laser heating can be divided into the steady-state and time-dependent parts:

$$T_{\mathrm{sus}}(r,t) = T_{\mathrm{sus,st}}(r) + T_{\mathrm{sus,tr}}(r,t) \tag{S10}$$

where $T_{\mathrm{sus,st}}$ is the dimensionless steady-state temperature rise due to CW laser heating, expressed as

$$T_{\mathrm{sus,st}}(x) = \frac{\theta_{\mathrm{sus,st}}(r)}{\eta P/(\pi\lambda_{\mathrm{sus}}b)} = \frac{1}{2}\ln\left(\frac{x_d}{2x}\right) + \frac{\mathrm{Ei}(-x^2) - \mathrm{Ei}(-x_d^2/4)}{4} - \pi\xi\left(\exp\left(-\frac{x_d^2}{4}\right) - 1\right) \tag{S11}$$

And the time-dependent part, $T_{\mathrm{sus,tr}}$, is expressed as

$$T_{\mathrm{sus,tr}}(x,\tau) = -\sum_{n=1}^{\infty} C_n J_0(\mu_n x)\exp\left(-\mu_n^2 Fo_{\mathrm{sus}}\tau\right) \tag{S12}$$

where C_{n} is given by

$$C_n = \frac{8\int_0^{x_d/2} T_{\mathrm{sus,st}}(x) J_0(\mu_n x) x\,dx}{x_d^2\left[(1+2\pi\xi)J_1(\mu_n x_d/2)^2 + J_0(\mu_n x_d/2)\left(J_0(\mu_n x_d/2) - J_2(\mu_n x_d/2)\right)/2\right]} \tag{S13}$$

And μ_{n} is the positive root of the following equation:

$$\pi\xi\mu_n x_d J_1(\mu_n x_d/2) - J_0(\mu_n x_d/2) = 0 \quad (\mu_n > 0, n = 1, 2, \ldots) \tag{S14}$$

Because the Gaussian radius of the laser spot is much less than the suspending radius, the Raman-measured temperature rise is expressed as the Gaussian-weighted-average value within the suspending area; that is,

$$\overline{\theta_{\mathrm{sus}}(r,t)} = \frac{\int_0^{t_{\mathrm{h}}}\int_0^{d/2}\theta_{\mathrm{sus}}(r,t)\exp\left(-r^2/r_0^2\right)r\,dr\,dt}{t_{\mathrm{h}}\int_0^{d/2}\exp\left(-r^2/r_0^2\right)r\,dr} \tag{S15}$$

Thus the Raman-measured steady-state temperature rise divided by the characteristic temperature rise is a function of x_d and ξ; that is,

$$\frac{\overline{\theta_{\mathrm{sus,st}}(r)}}{\eta P/(\pi\lambda_{\mathrm{sus}} b)}=\frac{2}{1-\exp\left(-x_d^2/4\right)}\int_0^{x_b/2} T_{\mathrm{sus,st}}(x)\exp\left(-x^2\right)xdx=f_{2,\mathrm{st}}\left(\frac{d}{r_0},\lambda_{\mathrm{sus}}R_{\mathrm{c}}b\right) \quad \text{S(16)}$$

And the Raman-measured temperature rise for pulsed laser heating divided by the characteristic temperature rise is a function of x_d, ξ and Fo:

$$\begin{aligned}\frac{\overline{\theta_{\mathrm{sus}}(r,t)}}{\eta P/(\pi\lambda_{\mathrm{sus}} b)}&=\frac{2}{1-\exp\left(-x_d^2/4\right)}\left[\begin{array}{l}\displaystyle\int_0^{x_b/2} T_{\mathrm{sus,st}}(x)\exp\left(-x^2\right)xdx\\ \displaystyle-\sum_{n=1}^{\infty} C_n\int_0^{x_b/2} J_0(\mu_n x)\exp\left(-x^2\right)xdx\\ \displaystyle\times\frac{1-\exp\left(-\mu_n^2 Fo_{\mathrm{sus}}\right)}{\mu_n^2 Fo_{\mathrm{sus}}}\end{array}\right] \quad \text{S(17)}\\ &=f_2\left(\frac{d}{r_0},\lambda_{\mathrm{sus}}R_{\mathrm{c}}b,\frac{\alpha_{\mathrm{sus}}t_{\mathrm{h}}}{r_0^2}\right)\end{aligned}$$

Supplementary Note S6 | Uncertainty analysis

The measurement errors consist of the systematic error and the random error. We first evaluate the radiation heat loss for the suspended samples, for the maximum temperature rises of the suspended samples were as high as 142 K to 341 K. The radiation heat loss is expressed as $Q_{\mathrm{r}} = \varepsilon\sigma A(T^4\text{-}T_0^4)$, where ε, σ and A respectively denote the emissivity, Stefan-Boltzmann constant and suspended graphene area, and T and T_0 are the temperatures of graphene and the environment, respectively. Taking ε = 1, T_0 = 300 K and T = 700 K, which corresponds to ~ 10 mW incident laser power based on the experimental results, Q_{r} is calculated to be 0.37μW for a 6μm diameter suspended sample. On the other hand, the laser absorption is 0.2mW taking the laser absorptivity as 0.02, thus the radiation heat loss is 0.19% of the laser absorption even when ε = 1 and the temperature rise is 400 K. Therefore, the radiation heat loss is negligible for all the measured samples.

According to the heat conduction models, the thermophysical properties of graphene are implicit functions of the Raman-measured temperature rise, and the variable laser spot radius and pulse durations, which are the main sources of uncertainty; that is,

$$\frac{\delta\Lambda}{\Lambda}\approx\sqrt{\left(\frac{\partial\ln\Lambda}{\partial r_0}\delta r_0\right)^2+\left(\frac{\partial\ln\Lambda}{\partial t_{\mathrm{h}}}\delta t_{\mathrm{h}}\right)^2+\left(\frac{\partial\ln\Lambda}{\partial\theta}\delta\theta\right)^2} \quad \text{S(18)}$$

where Λ represents the measured thermophysical property and θ represents the Raman-measured temperature rise.

S6.1 Uncertainty from the laser spot size

The uncertainty of the laser spot radius was determined by repeatedly measuring the Gaussian-radius at the same sample z position. Fig. S2(b) presents the CNT G band intensity profile at z = 1.2μm and x = -1.2μm ~ 0.8μm (ion laser), with the y-direction scanning step set as 50 nm and the xy resolutions being 20nm. It should be firstly noted that the y coordinates of the strongest G band

signals were exactly the same at different x positions, indicating that the individual CNT was perpendicular to the y direction. At seven different x positions, the CNT G band intensity profiles were almost the same and the Gaussian fitted spot radii were (312+5/-7) nm, with the standard deviation of the fitted Gaussian radii being 1.3% and the correlation coefficients of the Gaussian fitting larger than 0.998, thus the uncertainty of the laser spot radius from Gaussian fitting is taken as 1.3%. The z positioning resolution is another factor that contributes to the uncertainty of the laser spot radius at a given z position. The positioning resolution in the z direction is 100 nm, causing 0.48% ~ 3.8% spot size uncertainty for the ion laser and 1.3% ~ 5.0% spot size uncertainty for the diode laser when the spot radii vary between ~250 nm to ~1 μm, so the total uncertainty of the laser spot radius is about 5% and the thermal property uncertainty propagated from the spot sizes were estimated to be less than 10%.

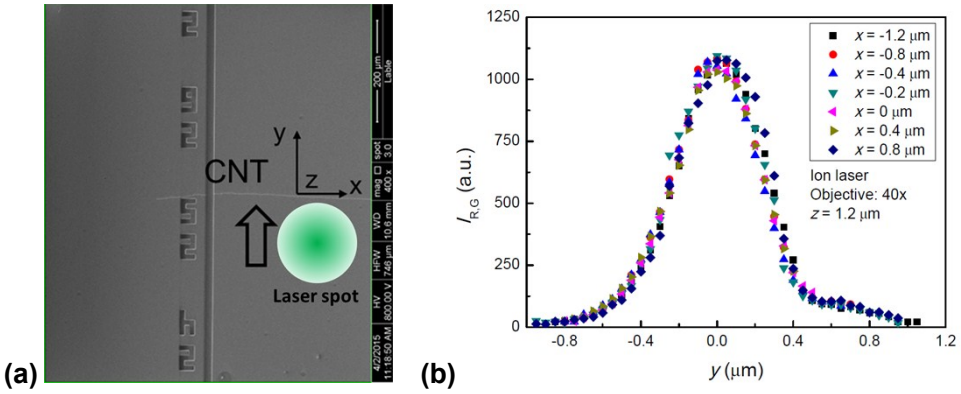

FIGURE S2. Repeated measurements for the incident laser spot radius at the same sample z position. (a) SEM image of the carbon nanotube and the schematic of the scanning coordinates. (b) CNT G band intensity profile at z = 1.2 μm, measured at different x positions.

S6.2 Uncertainty from the pulse duration

The square pulsed laser was generated by digitally modulating the diode laser (Omicron LuxX+ 488-200) with a delay generator (Stanford Research DG645, rise/fall time < 2 ns). The pulse width was set as 10 ns to 80 ns while the pulse interval was set as 10 times of the pulse width in our thermal measurements. This laser equipment was also modulated by Agilent 81160A (rise/fall time = 1.0 ns) in the laser company and the laser pulse waveforms were read by an optical-to-electrical converter and an oscilloscope, showing that the rise/fall time of the modulated laser pulse is about 1 ns (Fig. S3). Therefore, the rise/fall time of the modulated laser pulse can be limited by the rise/fall time of the delay generator, i.e. less than 2 ns in our experiment. Since the typical pulse width is ~50 ns, the uncertainty of the pulse width is ~ 4%, causing ~4% uncertainty in the thermal diffusivity.

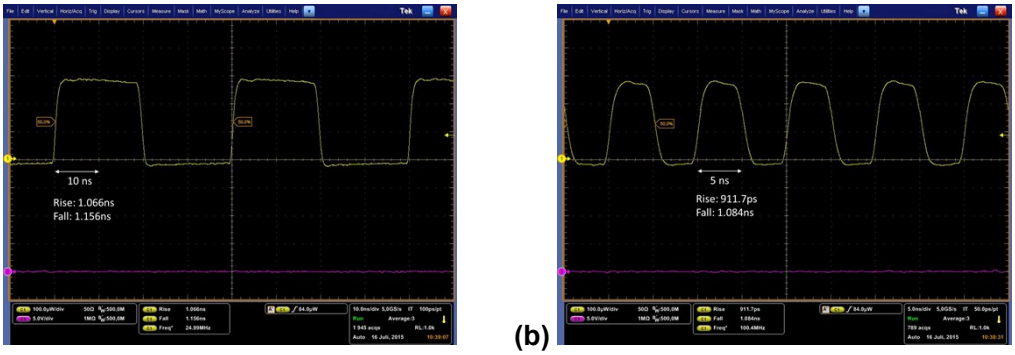

FIGURE S3. Test results of the digitally modulated pulsed laser waveform. (a) Pulse width = 20 ns, rise time = 1.066 ns, fall time = 1.156 ns. (b) Pulse width = 5 ns, rise time = 911.7 ps, fall time = 1.084 ns.

Besides, the extinction ratio of the digitally modulated laser is larger than 250:1, which means the laser-on power of the square pulsed laser is larger than 250 times of the laser-off power. We also detected the laser power in both CW mode and digital modulation mode using a laser power meter, showing that the average power of the pulsed laser can be accurately predicted by the CW power, pulse duration and period, thus the uncertainty from the extinction ratio is negligible.

S6.3 Uncertainty from the Raman-measured temperature

The random uncertainty of the Raman-measured temperature rises can contribute the largest part of uncertainty in the thermophysical properties. The temperature dependence of the Raman 2D band shifts is about -0.05 cm^{-1}/K and the spectrum resolution of the Raman spectrometer (Horiba T64000) is 0.15 cm^{-1}, while the random errors of the temperature rises were determined from repeated temperature measurements for 6 ~ 10 times, presented by the error bars in the data figures. For the supported samples, the random temperature errors were 2~4 K and the uncertainties of the temperature rises were 5% ~ 10% for CW heating and 9%~21% for pulsed laser heating, as the temperature rises were relatively low (steady-state temperature rises: 20 ~ 40 K). For the suspended samples, the random temperature errors were about 5 K and the uncertainties of the temperature rises were within 5%, for the maximum temperature rises were as high as 150 ~ 350 K. In order to reduce the random uncertainty from the temperature data, the thermophysical properties were extracted from several scattered temperature rise ratios by least squares fitting. The experimental data scattered around the best theoretical fitting curves and this data scattering can also add to the uncertainty of the fitting results, which is related to the correlation coefficients of the fitting and can be reduced by increasing the data point quantity. We estimate that the random uncertainty and scattering of the temperature rises result in 15% uncertainty in the extraction of thermal conductivity, interfacial or contact thermal resistance for CW laser heating, 30% uncertainty of thermal diffusivity for the supported samples and 20% uncertainty of thermal diffusivity for the suspended samples.

In summary, considering the uncertainty from the laser spot sizes, pulse durations and Raman-measured temperature rises, we estimate the total uncertainty to be within 20% for the best-fitted thermal conductivity, interfacial thermal conductance and thermal contact resistance, and within 30% for thermal diffusivity. On the other hand, the specific heat of graphene was

calculated from the extracted thermal conductivity and thermal diffusivity of the same sample, and the result is in accordance with the theory, which verified the accuracy of the measurement. Compared with the literature, we have improved the accuracy of Raman-based measurements by eliminating the uncertainty from laser absorption in the present work. In the future work, we can further improve the measurement accuracy by optimizing the data quantity and range, controlling the maximum sample temperature rise, using a more precise positioning sample stage and reducing the transition time of the laser pulses.

References

[1] Yener Y, Kakaç S. Heat conduction, 4th ed. New York: Taylor & Francis, 2008.

[2] Hull R (editor). Properties of crystalline silicon. London: INSPEC, the Institution of Electrical Engineers, 1999.